

# **Experimental Investigations of Multiphase Flow and Trapping in Saline Aquifers - Annual Report 2007 -**

**Sally M. Benson, Jean-Christophe Perrin, Michael Krause, Chia-Wei Kuo, and  
Ljuba Miljkovic**

**Department of Energy Resources Engineering  
School of Earth Sciences  
Stanford University**

**May 30, 2008**

## **Contacts**

Sally M. Benson: [sembenson@stanford.edu](mailto:sembenson@stanford.edu)

Jean-Christophe Perrin: [perrin@stanford.edu](mailto:perrin@stanford.edu)

Michael Krause: [krausm2@stanford.edu](mailto:krausm2@stanford.edu)

Ljuba Miljkovic: [ljuba@stanford.edu](mailto:ljuba@stanford.edu)

Chia-Wei Kuo: [chiaweik@stanford.edu](mailto:chiaweik@stanford.edu)

This work was supported by the Global Climate and Energy Project at Stanford University.

## Abstract

Our research focuses on the fundamental science underpinning sequestration in saline aquifers. Saline aquifers have the largest sequestration capacity, as compared to oil and gas reservoirs or deep unminable coal beds. Saline aquifers are also more broadly distributed and thus, closer to more emission sources. However, unlike oil and gas reservoirs with proven seals that have withstood the test of time, saline aquifers must be carefully characterized to assure that CO<sub>2</sub> will achieve high retention rates. Improved fundamental understanding of multi-phase flow and trapping in CO<sub>2</sub>-brine systems will be needed to take advantage of this large storage capacity of saline aquifers. Important questions remain to be answered, such as, what fraction of the pore space will be filled with CO<sub>2</sub>, what will be the spatial extent of the plume of injected CO<sub>2</sub>, how much and how quickly will CO<sub>2</sub> dissolve in brine, and how much CO<sub>2</sub> will be trapped by capillary forces when water imbibes back into the plume and to what extent is capillary trapping permanent? To date, these questions have largely been addressed through the use of numerical simulators. Here we are developing new experimental data to improve our ability to answer these questions.

We are carrying out core-scale multi-phase flow experiments to investigate the fundamental processes that underpin these questions. Each set of experiments involves co-injecting CO<sub>2</sub> and brine at a range of fractional flows and a number of different total flow rates. X-ray CT scanning is used to map the spatial distribution of CO<sub>2</sub> and brine. Detailed petrophysical analysis of the core is used to obtain 3-dimensional maps of porosity, permeability and capillary pressure. Rock properties are used to provide insight into the influence of spatial heterogeneity on the distribution of CO<sub>2</sub> and brine in the cores. Rock properties are also used as input to carry out high resolution numerical simulations of the core flood experiments. Early experiments demonstrated that during drainage, the spatial distribution of saturation within the core is large, even for rocks that are fairly homogeneous. Simulations of these experiments demonstrate that the spatial heterogeneity could not be explained by porosity and permeability variations. Instead, only spatial variations in capillary pressures could explain the saturation patterns observed in the laboratory experiments. Based on these early results, we hypothesized that the efficiency of brine displacement and relative permeability curves could depend on the flow rate.

As our research progresses, we will assess which, if any, modifications to multiphase flow theory are needed to replicate the experiments and develop approaches for up-scaling laboratory measured relative permeability curves for use in reservoir-scale simulations.

## Contacts

Sally M. Benson: [smbenson@stanford.edu](mailto:smbenson@stanford.edu)

Jean-Christophe Perrin: [perrin@stanford.edu](mailto:perrin@stanford.edu)

Michael Krause: [krausm2@stanford.edu](mailto:krausm2@stanford.edu)

Ljuba Miljkovic: [ljuba@stanford.edu](mailto:ljuba@stanford.edu)

Chia-Wei Kuo: [chiaweik@stanford.edu](mailto:chiaweik@stanford.edu)

## Introduction

Carbon dioxide capture and sequestration (CCS) in deep geological formations has emerged over the past ten years as an important component of the portfolio of options for reducing greenhouse emissions. Three commercial projects now operating provide valuable experience for assessing the efficacy of CCS. To date, these projects are performing as expected, with no evidence for leakage or other unexpected difficulties. If CCS is implemented on the scale needed for large reductions in CO<sub>2</sub> emissions, a billion tonnes or more of CO<sub>2</sub> will be sequestered annually—a 250 fold increase over the amount intentionally sequestered annually today. Effectively sequestering these large volumes will require building a strong scientific foundation of the coupled hydrological-geochemical-geomechanical processes that govern the long term fate of CO<sub>2</sub> in the subsurface. In addition, we will need methods to characterize and select sequestration sites, subsurface engineering to optimize performance and cost, safe operations, monitoring technology, remediation methods, regulatory oversight, and an institutional approach for managing long term liability.

Our research focuses on the fundamental science underpinning sequestration in saline aquifers. Saline aquifers have the largest sequestration capacity, as compared to oil and gas reservoirs or deep unminable coal beds. Saline aquifers are also more broadly distributed and thus, closer to more emission sources. However, unlike oil and gas reservoirs with proven seals that have withstood the test of time, saline aquifers must be carefully characterized to assure that CO<sub>2</sub> will achieve high retention rates. Improved fundamental understanding of multi-phase flow and trapping in CO<sub>2</sub>-brine systems will be needed to take advantage of this large storage capacity of saline aquifers. Important questions remain to be answered, such as, what fraction of the pore space will be filled with CO<sub>2</sub>, what will be the spatial extent of the plume of injected CO<sub>2</sub>, how much and how quickly will CO<sub>2</sub> dissolve in brine, and how much CO<sub>2</sub> will be trapped by capillary forces when water imbibes back into the plume and to what extent is capillary trapping permanent? To date, these questions have largely been addressed through the use of numerical simulators. Here we are developing new experimental data to improve our ability to answer these questions.

Our laboratory is carrying out core-scale multi-phase flow experiments to investigate the fundamental processes that underpin these questions. Figure 1 illustrates the four interrelated components of our comprehensive approach. We are conducting transient and steady state core-flood experiments at representative reservoir pressure and temperatures. Each set of experiments involves co-injecting CO<sub>2</sub> and brine at a range of fractional flows and a number of different total flow rates. X-ray CT scanning is used to map the spatial distribution of CO<sub>2</sub> and brine. Detailed petrophysical analysis of the core is used to obtain 3-dimensional maps of porosity, permeability and capillary pressure. Rock properties are used to provide insight into the influence of spatial heterogeneity on the distribution of CO<sub>2</sub> and brine in the cores. Rock properties are also used as input to carry out high resolution numerical simulations of the core flood experiments. In addition, traditional steady state relative permeability measurements have been made during drainage and imbibition. As our research progresses, we will assess which, if any, modifications to multiphase flow theory are needed to replicate the experiments and develop approaches for up-scaling laboratory measured relative permeability curves for use in reservoir-scale simulations.

Early experiments demonstrated that during drainage, the spatial distribution of saturation within the core is large, even for rocks that are fairly homogeneous. Simulations of these experiments demonstrate that the spatial heterogeneity could not be explained by porosity and permeability variations. Instead, only spatial variations in capillary pressures could explain the saturation patterns observed in the laboratory experiments. Based on these early results, we hypothesized that the efficiency of brine displacement and relative permeability curves could dependent on the flow rate. Subsequent experiments were carried out at a range of flowrates to investigate this hypothesis.

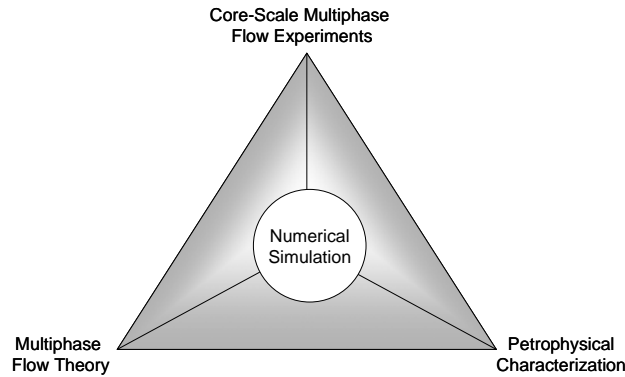


Figure 1: Illustration of the 4 interrelated components of our approach to study multiphase flow and trapping in saline aquifer.

Follow-on experiments have confirmed observations from the initial core-flood experiments—that the spatial distribution of CO<sub>2</sub> saturation is highly variable and correlated to the properties of the rock. Efficient brine displacement occurs in regions with high porosity, high permeability and low capillary pressures. Regions of the core with lower porosity, permeability and high capillary pressures are difficult to invade with CO<sub>2</sub>. The experiments also demonstrate that brine displacement efficiency is flow rate dependent, as are the relative permeability curves. At higher flowrates, brine displacement is more efficient than at lower flow rates.

This report has four sections. Section 1 describes the new laboratory that we have built for carrying out these experiments, including some of initial data sets we have collected. Section 2 describes the approach we are taking for the sub-core scale characterization of porosity, permeability and capillary pressure that is needed as input for simulating the core-scale experiments. Section 3 describes the simulation work. Section 4 describes a web-based application for collecting and providing relative permeability curves for CO<sub>2</sub>-brine systems.

# 1. Multiphase Flow Experiments

Jean-Christophe Perrin: [perrin@stanford.edu](mailto:perrin@stanford.edu), Sally M. Benson: [sembenson@stanford.edu](mailto:sembenson@stanford.edu)

## 1.1 Experimental setup

A new experimental setup has been designed for two phase core flooding experiments (Figure 2). The core sample is wrapped in a Teflon sleeve and is placed in an aluminum core holder. A pump (Pump D) injects water around the sleeve to create the overburden pressure (reservoir pressure). Two electric heaters heat the water inside the core holder to maintain the core at the reservoir temperature. Two dual-pump systems are used to inject brine and CO<sub>2</sub> in the core sample (Pumps A1 & A2 for CO<sub>2</sub> and B1 & B2 for brine). Both of them are composed of two pumps connected with a set of electric valves. The dual pump configurations provide continuous fluid delivery by synchronizing the pump and refill strokes so that at least one pump is always delivering fluid. Electric valves support automated functions and are ideal for CO<sub>2</sub> application.

The CO<sub>2</sub> pumps are surrounded by a water-cooled temperature jacket. The temperature control jacket allows fast and complete filling of the cylinder when pumping liquefied CO<sub>2</sub>. Before entering the core, CO<sub>2</sub> and brine pass through a water bath (heat exchanger) to be heated at the reservoir temperature. They are then mixed and co-injected in the core. After having flown through the core, CO<sub>2</sub> and brine are separated by gravity in a high pressure separator. The CO<sub>2</sub> returns back to the CO<sub>2</sub> pump system and the brine is conducted back to the brine pump system. Between the separator and the CO<sub>2</sub> pump system, a pump (Pump C) is used to maintain the back pressure. The back pressure, also called working pressure or pore pressure, is always at least 200 psi below the overburden pressure value to avoid any leakage through the Teflon sleeve surrounding the core. This pump is used as a buffer volume as well.

Due to the dual pumps systems, CO<sub>2</sub> and brine are circulated continuously in the system. Thus the two fluids are in constant contact with each guaranteeing the CO<sub>2</sub> to be brine saturated and the brine to be CO<sub>2</sub> saturated. This precaution is meant to avoid any drying the core, which is often encountered when dry CO<sub>2</sub> (not saturated with brine) is injected.

During the experiments, the pressure drop across the core is measured with two high accuracy pressure transducers. The temperature inside the core holder, the pressure drop, the injection flow rate, the injection pressure and the volume of each pumps are measured and recorded. The entire setup, despite its size, is easily movable and can be transported to a CT room where X-ray CT scanning is used to measure CO<sub>2</sub> and brine saturations.

## 1.2. Conditions and Experimental Procedures

The experimental apparatus allows performing experiments on rock samples at reservoir conditions. The temperature ( $50 \pm 0.1$  C) and the pore pressure (1700 psi / 12.4 MPa) was chosen for the first experiments. The rock sample is a 5.08 cm diameter by 15.24 cm long Berea Sandstone cylinder.

The absolute permeability of the core was measured by injecting a brine solution composed of 10 000 ppm NaCl at different flow rates. Using Darcy's law, the value of the permeability at these experimental conditions is measured at  $430 \pm 7$  md.

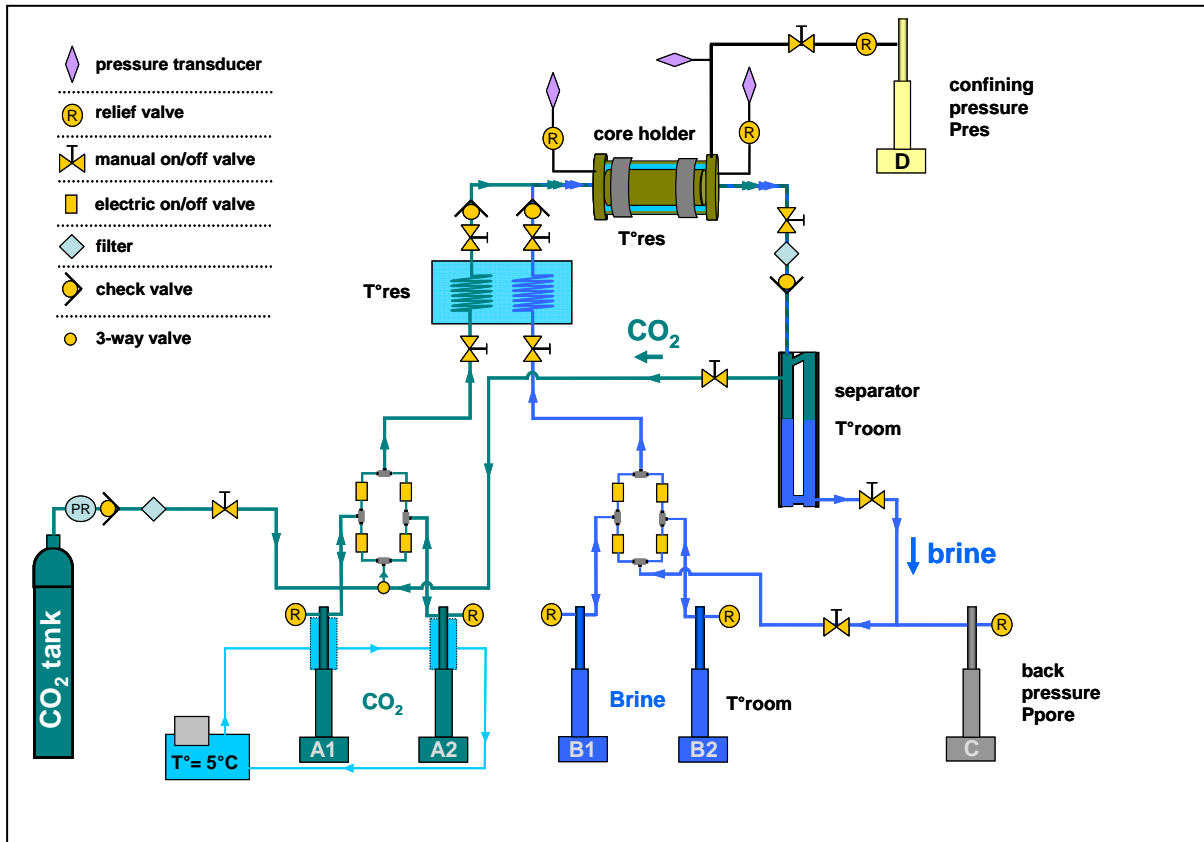


Figure 2: Core flooding experimental setup. The rock sample is maintained at reservoir pressure and reservoir temperature. CO<sub>2</sub> and brine circulate in a closed loop.

At such high pressure and temperature, CO<sub>2</sub> is supercritical and brine is liquid. The density ratio between the two fluids is 3.5 and the viscosity ratio 12.1 (see Table I). The Bond number, calculated using the relation (1.1), is  $2.2 \cdot 10^{-3}$  for a CO<sub>2</sub> – brine interfacial tension of  $\sigma = 30$  dyne/cm. The  $\sigma$  value corresponds to what is commonly measured in CO<sub>2</sub> / brine systems at these conditions. [1]

$$Bo = \frac{\Delta\rho L^2 g}{\sigma} \quad (1.1)$$

The low value of  $\sigma$  indicates that surface tension dominates over gravitational effects during the experiments.

Table I: Physical properties of CO<sub>2</sub> and brine at experimental conditions.

	State	Density (g/cm <sup>3</sup> )	Density ratio	Viscosity (cP)	Viscosity ratio
CO <sub>2</sub>	supercritical	0.28	3.5	0.046	12.1
brine	liquid	0.99		0.558	

### 1.3. Procedure for Two-Phase Flow Experiments

The two-phase flow experiments have been performed at three different volumetric flow rates (FR). FR corresponds to the sum of the volumetric flow rate of CO<sub>2</sub> at 50 C and the volumetric flow rate of brine at 50 C. We chose a range of flow rates which correspond to those anticipated in the storage reservoir both near and distant from the injection well: 2.6 mL/min, 1.2 mL/min and 0.5 mL/min. The experiments correspond to drainage conditions (the core is initially saturated with brine) and the measurements of the pressure drop across the core and the saturations are done at steady state. The following procedure has been used:

-1- Co-inject CO<sub>2</sub> and brine at a given fractional flow  $f_{CO_2}$ .  $f_{CO_2}$  is defined as the ratio of the volumetric flow rate of CO<sub>2</sub> and the total volumetric flow rate FR.

$$f_{CO_2} = \frac{FR_{CO_2}}{FR} = \frac{FR_{CO_2}}{FR_{CO_2} + FR_{brine}}, \quad f_{brine} = \frac{FR_{brine}}{FR} = 1 - f_{CO_2} \quad (1.2)$$

-2- Wait for steady state conditions. The steady state is reached when both pressure drop and saturations are stabilized. It often takes 5-7 pore volumes, depending on the flow rate. All the measurements have been done after having flown 8 to 10 pore volume of fluids.

-3- Measurement of pressure drop and saturations of CO<sub>2</sub> and brine.

-4- Incrementally increase the fractional flow of CO<sub>2</sub>.

The last three steps are repeated until only CO<sub>2</sub> is flowing. Then the *exact same initial state* (core saturated with brine) is recovered and the exact same procedure is followed at a different total flow rate FR. The range of the total flow rates [2.6-0.5 mL] corresponds to a range of capillary numbers  $[2-12] \times 10^{-6}$ . The capillary numbers are calculated using relation (1.3) where  $\mu$  is the viscosity of the more viscous fluid (brine) and S is the surface exposed to the flow ( $S = 40.53 \text{ cm}^2$ ).

$$Ca = \frac{FR\mu}{S\sigma} \quad (1.3)$$

### 1.4. Porosity and Saturation Maps from X-Ray CT Images

A medical X-ray CAT scanner is used to map saturations in the core during the experiments. The scanner creates 2-D saturation maps at each location along the length of the sample. To scan the entire core we need to take 29 2-D maps with a gap of 2.08 mm between consecutive images. The 3-D saturation maps are then constructed by stacking the 2-D images along the third dimension. Each slice is 3 mm thick. The X-Y resolution is 0.3 mm\*0.3 mm so that the voxel size is 0.3 \* 0.3 \* 3 mm<sup>3</sup>.

- Two sets of images are needed to obtain the porosity map: the dry images and the brine saturated images. The porosity of each voxel element is then calculated using [2]:

$$\Phi = \frac{CT_{brine}^{sat} - CT_{dry}}{CT_{brine} - CT_{air}} \quad (1.4)$$

where CT is a numerical value converted by the console from the X-ray attenuation coefficients. The CT numbers are normalized values relative to the linear coefficient of water.

- To obtain the saturation maps at each CO<sub>2</sub> fractional flow we need to take three sets of images: the brine saturated images, the CO<sub>2</sub> saturated images and the experimental images at steady state at each fractional flow. The CO<sub>2</sub> and brine saturations are then calculated for each voxel using [2]:

$$S_{\text{CO}_2} = \frac{CT_{\text{exp}} - CT_{\text{brine}}^{\text{sat}}}{CT_{\text{CO}_2}^{\text{sat}} - CT_{\text{brine}}^{\text{sat}}} \quad \text{and} \quad S_{\text{brine}} = 1 - S_{\text{CO}_2} \quad (1.5)$$

## 1.5. Results

### *Porosity*

The 3-D map of the porosity is shown Figure 3, left. The spatial distribution of the porosity appears to be clearly heterogeneous. The bedding is distinctly observed to be diagonal to the axis of the core. Although the rock appears to be heterogeneous in terms of porosity, the porosity profile (Figure 3, right) is relatively flat. Each dot represents the slice-averaged value of the porosity along the sample. The mean core porosity value is measured to be  $\Phi = 0.203$ .

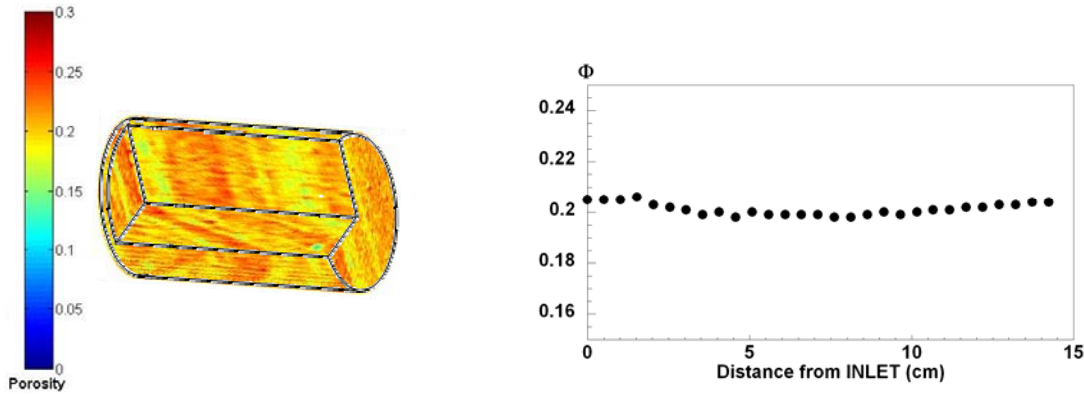


Figure 3: Left: 3-D map of the core porosity. Right: Porosity profile along the core.

### *Two-phase flow experiments*

In Figure 4 the slice averaged CO<sub>2</sub> saturation is plotted as a function of the distance from the inlet of the core sample for each total flow rate (Figure 4 a), b) and c)). Each curve corresponds to a different fractional flow. All the measurements have been made at steady state.

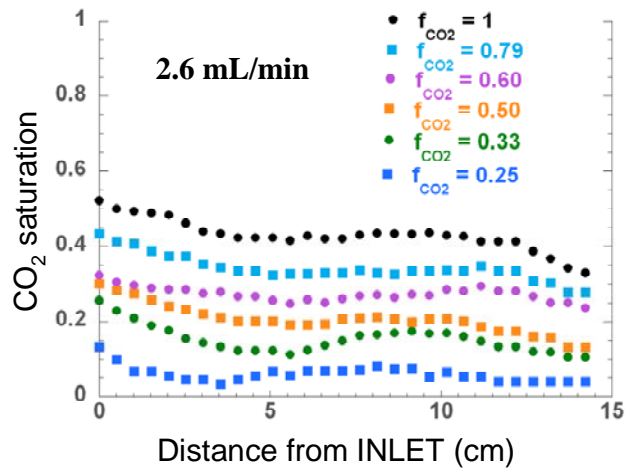


Figure 4 a): CO<sub>2</sub> saturation for different fractional flow at a total flow rate FR=2.6 mL/min.

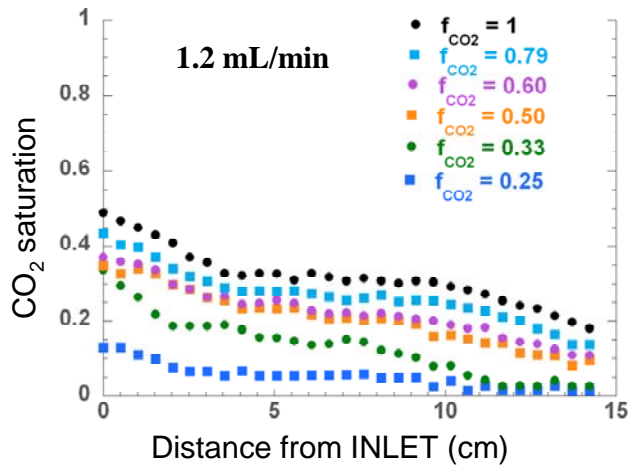


Figure 4 b): CO<sub>2</sub> saturation for different fractional flow at a total flow rate FR=1.2 mL/min.

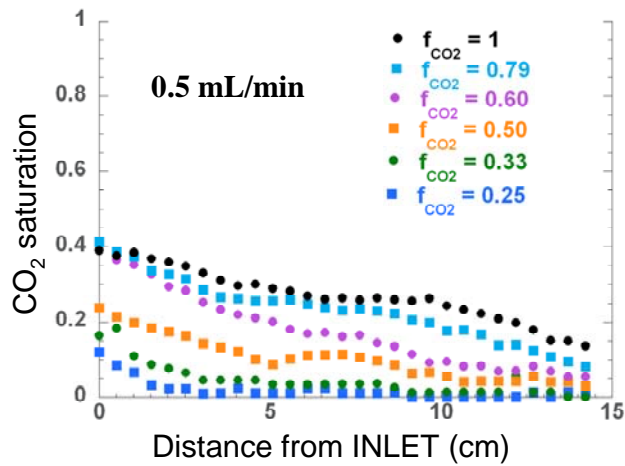


Figure 4 c): CO<sub>2</sub> saturation for different fractional flow at a total flow rate FR=0.5 mL/min.

The comparison between Figures 4 a), b), and c) clearly shows a dependence of the CO<sub>2</sub> saturation on the flow rate. A lower flow rate always leads to a lower saturation independent of the fractional flow. This effect is more visible for high fractional flows. In Figure 5 the averaged core values of the CO<sub>2</sub> saturation are plotted as a function of the flow rate for the different fractional flow. The deviation from the “standard” Buckley Leverett theory is distinctly observed for each value of the fractional flow.

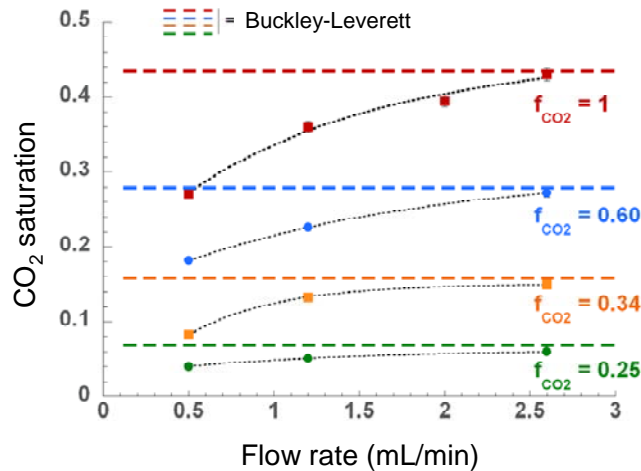


Figure 5: Core averaged CO<sub>2</sub> saturation as a function of flow rate for different CO<sub>2</sub> fractional flow. The experimental values are compared with the prediction of the Buckley-Leverett theory.

Figure 5 reveals unusually low values of the CO<sub>2</sub> saturation at the end of each experiment. At  $f_{CO_2} = 1$ , the saturation varies from 0.271 at 0.5 mL/min to 0.430 at 2.6 mL/min. At each different fractional flow the saturation seems to approach a plateau value, although the experiments have not been performed at a sufficiently high total flow rate to demonstrate this behavior with confidence. The spatial variations of the CO<sub>2</sub> saturation at the end of each experiment are shown on Figure 6, with blue corresponding to high CO<sub>2</sub> saturation and red to high brine saturation.

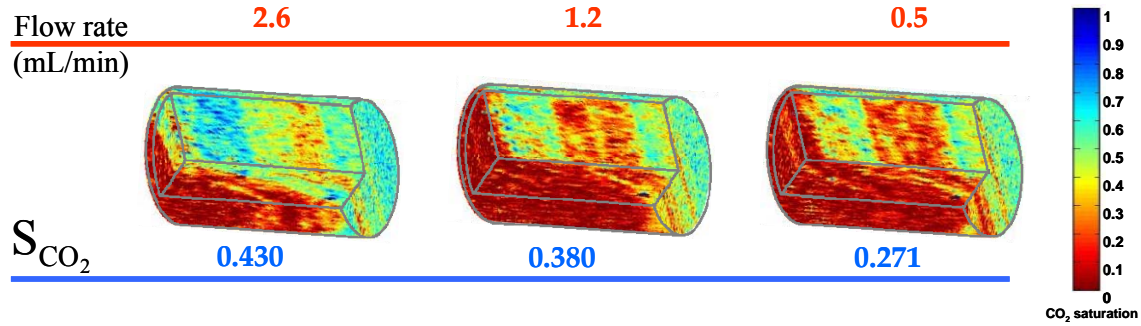


Figure 6: CO<sub>2</sub> saturation maps at the end of each experiment (end point). The mean CO<sub>2</sub> saturation for the entire core is indicated at the bottom of each 3D view.

The most striking observation is that, even at the end of each experiment when only CO<sub>2</sub> is flowing through the core, very large regions are poorly filled with CO<sub>2</sub> (e.g. bottom of the core, at the right side). These regions do not correspond to low porosity (or low permeability) regions. The comparison between the porosity map in Figure 3 and Figure 6 shows a poor correlation between porosity and saturation far from the inlet of the core (the inlet is on the right side of the image). However, the correlation is good close to the inlet face where high porosity corresponds to high CO<sub>2</sub> saturation. It appears that not only the spatial distribution of porosity (and thus permeability) is controlling the distribution of CO<sub>2</sub> but also the connectivity between the high porosity regions and the inlet face of the core where CO<sub>2</sub> is injected.

The dependence of the CO<sub>2</sub> saturation on the flow rates leads to a dependence of the relative permeability on the flow rate. Figure 7 shows the relative permeability curves measured at 2.6 and 1.2 mL/min. At 0.5 mL/min the pressure drop was unfortunately too small and the values too noisy to measure accurate relative permeability values.

Relative permeabilities are calculated using relation (1.6) where  $k$  is the measured absolute permeability,  $S$  the surface exposed to the flow (surface of the inlet face) and  $\Delta P$  the measured pressure drop across the core.

$$k_r^{\text{brine}} = \frac{\mu_{\text{brine}} FR_{\text{brine}}}{Sk\Delta P} \quad \text{and} \quad k_r^{\text{CO}_2} = \frac{\mu_{\text{CO}_2} FR_{\text{CO}_2}}{Sk\Delta P} \quad (1.6)$$

Although the shape and the trend of each set of curves stay qualitatively the same, we observe a dramatic shift toward lower values when the total flow rate decreases.

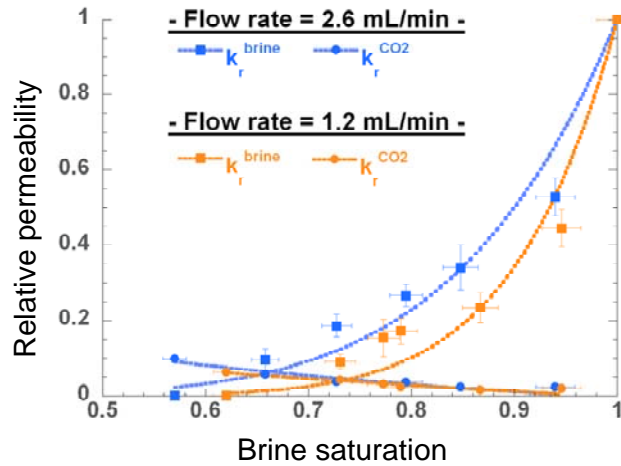


Figure 7: Relative permeability curves measured at 2.6 and 1.2 mL/min.

## 1.6. Discussion

### *Spatial distribution of CO<sub>2</sub>*

Although the core sample may appear homogeneous when analyzing the slice averaged porosity profile, the 3D view shows important spatial heterogeneities. As a consequence, the permeability map presents such heterogeneities. These spatial variations control the two phase flow: the CO<sub>2</sub> (non wetting phase) fills the high porosity/permeability regions when they are accessible to the flow. The low connectivity between high permeability regions and the inlet face of the core results in low CO<sub>2</sub> saturation in high permeability regions which is contrary to common expectations.

### *Influence of gravity*

Such a separation between different parts of the core could also be explained by gravity override. In this particular case, gravity effects do not seem to play a major role since the CO<sub>2</sub> saturation at the end of each experiment (Figure 6) is qualitatively the same at each flow rate. Gravity override is strongly flow rate dependant and segregates more CO<sub>2</sub> and brine when the flow rate is low which is not observed in our case. Furthermore, the simulations (see Section 3 of this report) show that gravity effect in these experimental conditions are only dominant for very low flow rate (<0.5 mL/min) and for a homogeneous sample. The best way to check this assumption would be to perform the same set of experiment with the core sample rotate 90° along its main axis. We plan to do this.

### *Flow rate dependence*

The flow rate dependence which is measured at any given CO<sub>2</sub> fractional flow can not be explained in the framework of the standard Buckley Leverett theory. A qualitative explanation can be drawn if we consider that each sub-core scale element possesses its

own capillary pressure curve, representative of its own permeability and porosity. At low flow rates, the low pressure drop does not exceed the high capillary entry pressure of low permeability regions, which results in a low CO<sub>2</sub> saturation. At higher flow rates, CO<sub>2</sub> can invade these regions, which results in higher CO<sub>2</sub> saturation. The influence of capillary pressure dependence of each sub-core scale element is tested in numerical simulations (see Section 3 of this report). The results are consistent with the laboratory experiments.

### **1.7. Future Plans**

The flow rate dependence has to be described more precisely with a variety of core samples. Experiments at both lower and higher flow rates are essential to completely measure the behavior of the saturation versus flow rate. Experiments at high flow rate should provide the plateau value of the saturation. Different experiments at different conditions in terms of temperature and brine composition are needed to evaluate the effects of these parameters on the steady state saturations.

Imbibition experiments are also planned to evaluate hysteresis effects and study capillary trapping.

### **1.8. References**

1. Bennion, B. and Bachu S., The impact of Interfacial Tension and Pore Size Distribution/Capillary Pressure Character on CO<sub>2</sub> Relative Permeability at Reservoir Condition in CO<sub>2</sub>-Brine Systems, SPE 99325-MS. Paper presented at the 2006 SPE/DOE Symposium on Improved Oil Recovery held in Tulsa, Oklahoma, U.S.A., 22-26 April 2006.
2. Akin, S. and Kovscek, A. R., Computed tomography in petroleum engineering research, Geological Society, London, Special Publications; 2003; v. 215; p. 23-38.

## 2. Petrophysical Analysis: Using Pore Scale Characteristics to Determine a Sub-Core Scale Permeability Distributions

Michael Krause: [krausm2@stanford.edu](mailto:krausm2@stanford.edu), Sally M. Benson: [sembenson@stanford.edu](mailto:sembenson@stanford.edu)

In order to model the experiments numerically, an accurate relationship is required to obtain the permeability distribution within the core. The only information available on sub-core scale properties is provided by the CT scanner, which only provides an average value of porosity for each pixel, so a relationship based on porosity is required. In early simulations we used the Carman-Kozeny equation shown in (2.1), where  $k_i$  is the permeability,  $S$  is determined empirically for the entire core and  $\Phi_i$  is the porosity of each discrete element in the CT scan of the core.

$$k_i = \frac{\Phi_i^3}{S(1 - \Phi_i)^2} \quad (2.1)$$

Numerical simulations conducted using this equation suggested that the permeability map needed to be improved to capture the spatial distribution of CO<sub>2</sub> saturations. The first step in improving the spatial correlation of CO<sub>2</sub> saturation between numerical simulations and the experiment is to improve the permeability relationship to include more information about the core. With this in mind, a different form of the Carman-Kozeny equation which includes additional physical characteristics of the rock is used (2.2).

$$k_i = \frac{c_0}{a_v^2} \frac{\Phi_i^3}{(1 - \Phi_i)^2} \quad (2.2)$$

This equation includes the factor  $c_0$ , which is again a constant determined for the entire core, but the magnitude of the constant is much closer to unity than the previous form. The other difference is  $a_v$ , which in three dimensions is a ratio of the surface area per unit volume of rock. This is a difficult quantity to measure because of the three dimensional nature of it, however, in two dimensions, a length can be factored out and it becomes a ratio between the sum of pore perimeters and grain areas in an imaged cross section.

In order to determine this parameter, thin section analyses have been used. Thin sections are usually used in petrographic analysis of rocks to study the minerals present, cementation of the rock grains, and to describe the porosity of the rock. A thin section is a rock sample which has been injected with dyed epoxy, allowed to harden, and then ground down to 30 microns thickness, it is then possible to see through mineral grains, but not the dyed epoxy. This image can then be transformed based on the colors present, since the pores are dyed blue, they can be isolated from the surrounding rock grains based on color and studied by doing the image conversion shown in Figure 8.

The image shown in Figure 8 is only a small sub-sample of a larger image. The rock grains are clearly identifiable in the color image. A computer program has been written which takes the color image as input, then using image analysis techniques, converts the multi-color image to a binary one.

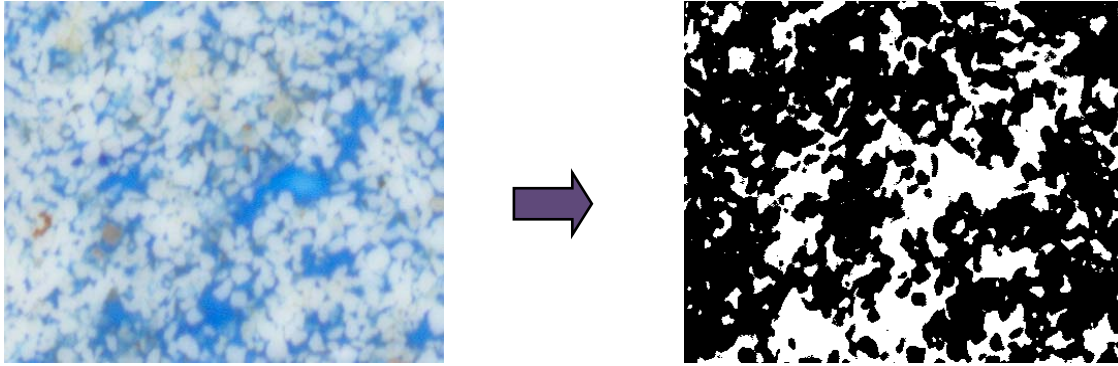


Figure 8: Thin section sample and binary conversion.

The full image is then discretized to correspond to the size of the CT pixel. An example is shown in Figure 9. In this experiment the length of each CT voxel was 3 mm and the height and width were 0.3 mm, therefore the black and white thin section is discretized to be the same size as the long face on a CT voxel (Figure9). The image is discretized by overlaying a cartesian grid and studying each unique element defined by the grid.



Figure 9: Example size of a discrete thin section element.

The computer program scans the image and processes each grid element to extract pore scale information. The porosity, total pore perimeter and total grain area are calculated for each element at the scale of the image shown in Figure 9. We can then use this information to calculate  $a_v$  in the equation discussed earlier, thus incorporating pore scale information into calculating permeability. By determining  $c_0$  for the core, the permeability of each discrete element can be determined to check the average calculated permeability of the composite thin section against what is measured for the core, in this way the precision of the method can be verified and calibrated as necessary. A typical thin section can be calculated to have exactly the same permeability as the measured core permeability by taking an arithmetic average of all of the discrete elements in the thin section.

In order to incorporate the information learned from the thin sections into developing sub-core scale permeability maps based on the CT images, we sought a relationship between the parameter  $a_v$  and porosity from the thin section data. By calculating  $a_v$  for each element in the entire thin section and the corresponding porosity of each element, a scatter plot can be created, shown below, which can be fitted with a regression line. This regression is expected to be unique for each different rock type or sample. The scatter plot and regression line for the thin section of Berea Sandstone is shown in Figure 10.

The  $R^2$  value of 0.87 for the regression line indicates that the fit is good, with only a modest amount of scatter.

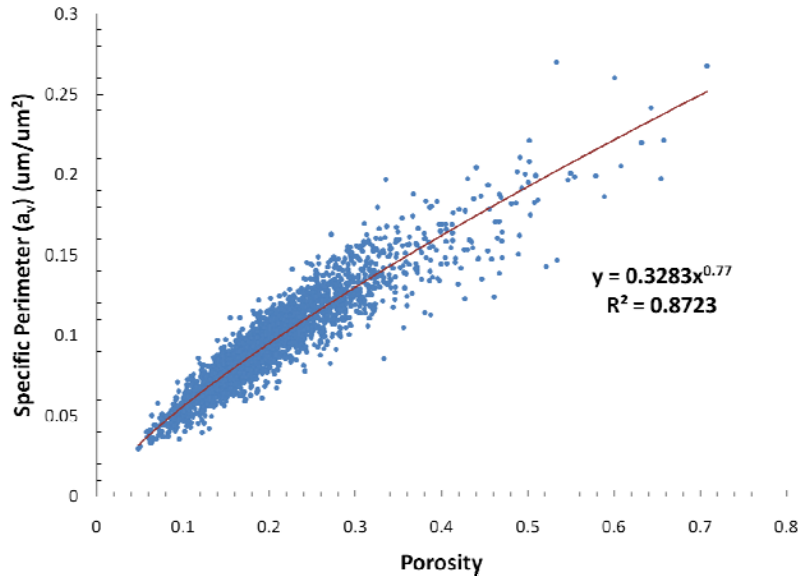


Figure 10: Scatter plot of  $a_v$  vs. porosity and regression line.

In this way, pore scale information can be taken from the thin section and made into a function of sub-pore scale information (porosity). Substituting this regression equation in for  $a_v$  gives the relation (2.3), which is only a function of porosity, but includes information about the pore scale physical properties of the core.

$$k_i = \frac{c_0}{(0.3283\Phi^{0.77})^2} \frac{\Phi_i^3}{(1 - \Phi_i)^2} \quad (2.3)$$

### Future Work

We will conduct tracer tests as an alternative approach for quantifying sub-core scale permeability distributions. The results from the two methods will be compared. In addition, this new relationship between porosity and permeability will be used to generate sub-core scale permeability maps for the core described in Section 1. Numerical simulations will then be carried out to compare the results from the CO<sub>2</sub> core-floods to calculated responses. These results will be compared to those calculated using the traditional Carman-Kozeny relationship to assess whether or not this new approach improves the match between simulated and measured core-flood experiments. If successful, we will use this same procedure to characterize other rocks and develop a general procedure for generating improved permeability maps by augmenting CT-scanning formation with thin-section data.

### 3. Numerical Simulations of Laboratory CO<sub>2</sub>/Brine Core-Floods

Ljuba Miljkovic: [ljuba@stanford.edu](mailto:ljuba@stanford.edu), Sally M. Benson: [smbenson@stanford.edu](mailto:smbenson@stanford.edu)

#### 3.1. Goals of the Simulation Studies

The goal of this work is to explain the origin of sub-core scale variations in CO<sub>2</sub> saturations observed during multi-phase flow experiments. The following simulations are based on a laboratory core flood conducted at Lawrence Berkeley National Laboratory, however the experimental method of injecting various proportions of CO<sub>2</sub> and brine is identical to that described in Section 1. These same procedures will be used to interpret the data provide in Section 1 and subsequent experiments.

Three-dimensional reconstructions of steady state CO<sub>2</sub> concentrations at a number for fractional flows show that the saturation distribution is highly variable, with regions remaining nearly 100% brine saturation even at high proportional flow rates of CO<sub>2</sub> (Figure 11).

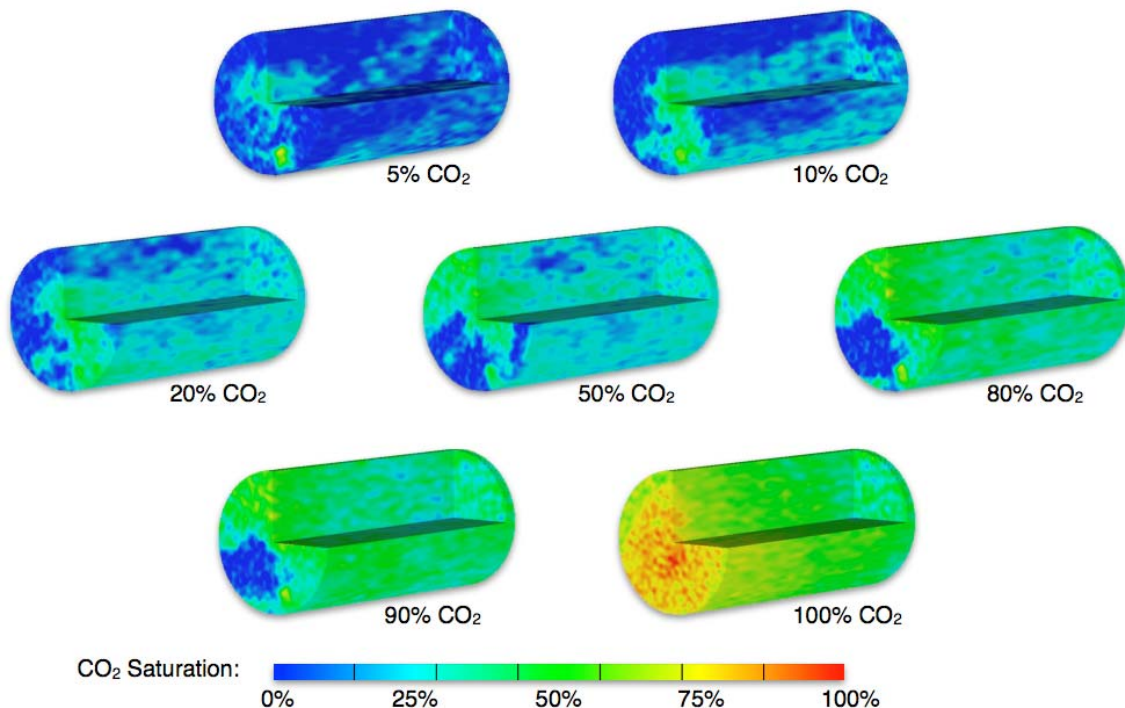


Figure 11: Three dimensional view of CO<sub>2</sub> saturation in the core at steady-state for each injection proportion. Variability at the inlet is likely due to non-uniform injection.

This degree of variability is surprising given the comparatively homogeneous nature of the Berea sandstone used for these experiments. Some of the variability at the inlet is likely the result of a non-uniform injection through the inlet-plate. CO<sub>2</sub> and brine may have separated in the space between the injection plate and the core face prior to entering the core. The focus of our simulations, however, is the smaller scale CO<sub>2</sub> saturation

variations found throughout the core—why they occur and what the underlying factors that control them are.

### 3.2. Description of the Numerical Simulations

The multi-phase flow simulator TOUGH2 MP with the ECO2N fluid property module was used to recreate these laboratory experiments. TOUGH2 MP is the multiprocessor version of TOUGH2 - a numerical simulator for flows of multicomponent, multiphase fluids in porous media. ECO2N was designed for applications in geologic sequestration of CO<sub>2</sub> in saline aquifers. It includes a comprehensive description of the thermodynamics and thermophysical properties of H<sub>2</sub>O - NaCl - CO<sub>2</sub> mixtures.

#### *Core Description and Grid Size*

The core used in these experiments is 3.83 cm in diameter and 7.78 cm long with a mean porosity of 22% and mean permeability of 310 mD. In order to simulate the core sample, the Berea's spatial porosity distribution was replicated in the simulation grid. CT scans of the core provided these data as a stack of 25 lateral images (180 pixel diameter) which represents a 3D map of porosity. Each voxel has a unique value of porosity and is of the dimensions 0.213·0.213·3.1 mm. The large “thickness” of each image was a limitation of the CT scanner available.

To obtain a permeability map for the simulation grid, the Kozeny-Carman relationship was applied to every pixel in the porosity map to create a new map of permeability values:

$$k_i = \frac{\Phi_i^3}{S(1 - \Phi_i)^2}$$

where  $k_i$  (mD) is a pixel value from the permeability map,  $\Phi_i$  is a pixel value in the porosity map,  $S$  is  $5.89292 \cdot 10^{-05} \text{ m}^{-2}$ , a factor such that the average of all permeability values in the map is equal to the bulk permeability of the core, 310 mD. We now have a roughly cylindrical simulation grid made of rectilinear elements, possessing 25 slices and 627,000 elements, each with a unique pair of porosity and permeability values. In the future we will use the approach for developing permeability maps outlined in Section 2.

#### *Initial and Boundary Conditions*

Identical hydrostatic initial conditions to those in the laboratory experiments were used for all simulations. The simulation temperature was held constant at 16°C. Because TOUGH2 cannot simulate the outlet pump itself, an outlet “slice” of infinite volume was added at the downstream end of the simulated core which would take up all injected fluid but remain at its initial pressure, 6.895 MPa. The outlet slice was placed out of capillary contact with the rest of the model by setting the capillary pressure gradient between the last slice of the core and the outlet slice to zero. By trial and error, this boundary condition was shown to most accurately replicate the observed saturation gradient in the core.

Prior to injection, all pore-space in the core was occupied by water with dissolved NaCl and CO<sub>2</sub>. Since TOUGH2 MP cannot model KI used in the laboratory experiments,

an equal mass fraction of NaCl (7.31%) was dissolved in the water instead. To saturate the brine with aqueous CO<sub>2</sub>, iterative preliminary simulations were performed to determine the maximum mass fraction of CO<sub>2</sub> that could be added to the brine before it exolved from solution. At the above initial conditions (6.895 MPa, 16°C) this mass fraction of CO<sub>2</sub> in brine is 4.54%.

To saturate the injected brine with aqueous CO<sub>2</sub>, additional CO<sub>2</sub> was co-injected beyond the amount indicated by the stated CO<sub>2</sub>/brine injection proportion. As with the initial brine in the core, CO<sub>2</sub> mass fraction of the injected brine was 4.54%. This prevents high CO<sub>2</sub> proportion injections from drying out the residual brine in the core.

As an additional input parameter, we used the core's capillary pressure curve, measured by Hg injection at an independent rock lab. A new capillary pressure function was used that provides a better curve fit to the measured data than does the traditionally used Leverett J-function. The capillary pressure ( $P_{c,i}$ ) of element  $i$  is calculate by scaling the new J-function by the square root of the element's porosity,  $\Phi_i$ , and permeability,  $k_i$  (Leverett scaling), and multiplying by the CO<sub>2</sub>-brine interfacial tension  $\sigma$ :

$$p_{c,i}(S) = \sigma \sqrt{\frac{\Phi_i}{k_i}} J(S)$$

where

$$J(S) = A \left( \frac{1}{S_*^{\lambda_1}} - 1 \right) + B (1 - S_*^{\lambda_2})^{1/\lambda_2}$$

$$S_* = \frac{S - S_p}{1 - S_p}$$

---

A = 0.003	B = 0.209	S <sub>p</sub> = 0.010	λ <sub>1</sub> = 3.6	λ <sub>2</sub> = 4.6
-----------	-----------	------------------------	----------------------	----------------------

---

and  $S$  is the brine saturation in the grid element. Figure 12 shows a plot of  $P_{c,i}$  versus  $S$ .

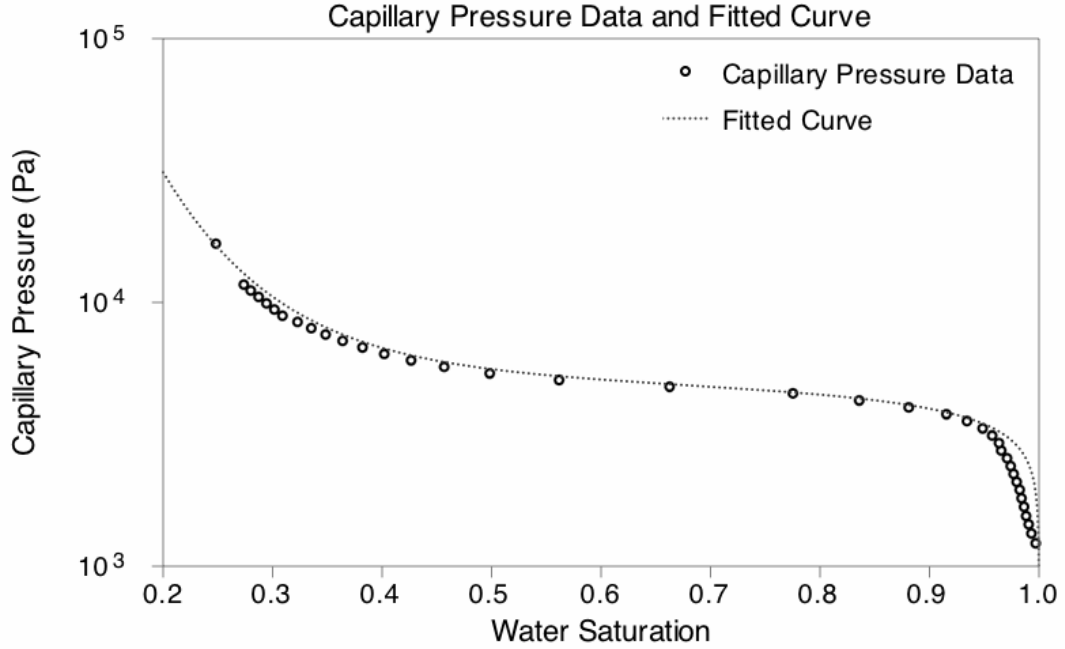


Figure 12: Laboratory capillary pressure data with curve fit used in simulations.

The relative permeability curves for brine and CO<sub>2</sub> used as inputs to the TOUGH2 model (Figure 13) were fit to data measured in the lab using the following power-law functions:

$$k_{r,CO_2} = \left( \frac{1 - S_{br}}{1 - S_{br,r}} \right)^{n_{CO_2}} \quad k_{r,br} = \left( \frac{S_{br} - S_{br,r}}{1 - S_{br,r}} \right)^{n_{br}}$$

---


$$S_{br,r} = 0.36$$

$$n_{CO_2} = 3.7$$

$$n_{br} = 3.5$$


---

where  $S_{br}$  is the average brine saturation,  $S_{br,r}$  is the residual brine saturation,  $n_{br}$  and  $n_{CO_2}$  are the functional exponents for the brine and CO<sub>2</sub> curves respectively, and the residual CO<sub>2</sub> saturation is zero.

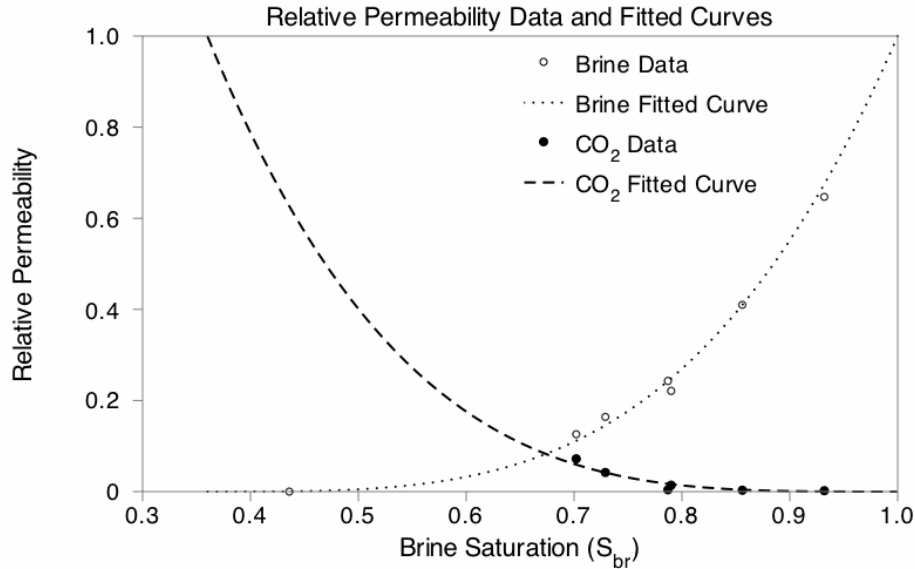


Figure 13: Relative permeability curves for CO<sub>2</sub> and brine fitted to experimental data.

Finally, to make the simulations more computationally tractable, the number of elements was decreased by reducing the lateral resolution of the grid. Local averages of the porosity and permeability data reduced the original resolution (180 pixel diameter) to a grid of a 60 pixels in diameter while keeping the physical dimensions the same.

### Results and Discussion

The first simulation scenario employed a completely homogeneous core, with averages values of porosity and permeability: 22% and 301 mD, respectively. For all three injection proportions the CO<sub>2</sub> saturation was uniform throughout the core.

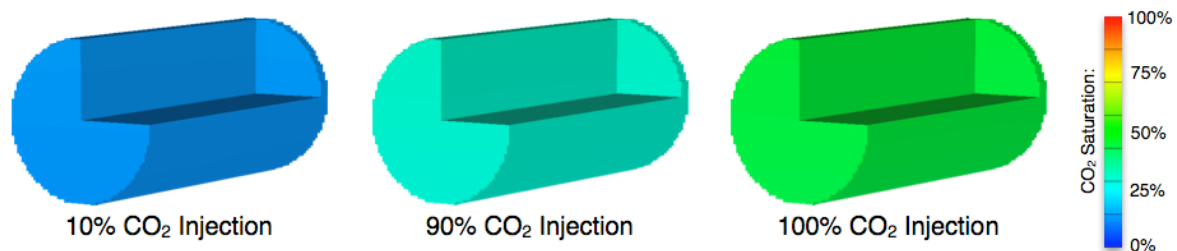


Figure 14: CO<sub>2</sub> saturations of simulated homogeneous core is completely uniform.

As expected, higher CO<sub>2</sub> injection proportions produce higher CO<sub>2</sub> saturations in the core (Table 3.1). Saturation profiles show a uniform distribution of CO<sub>2</sub> through the core (Figure 14). There is no gravity segregation of CO<sub>2</sub> and brine at these flow rates.

In the second simulation scenario, the same three injection trials were performed on a heterogeneous core that conformed to the original porosity and permeability maps. However, Leverett scaling was not applied to the core on an element-by-element basis. Instead, a single capillary pressure curve was used - scaled by the core's average porosity and permeability - in all grid elements. The capillary pressure defined for each grid element was thus the same as that of the homogeneous scenario above, even though

porosity and permeability were variable. This isolates porosity and permeability variability as the potential cause of the sub-core scale heterogeneity observed in the lab scans.

Simulation results (Figure 15) show that in spite of a heterogeneous porosity and permeability, CO<sub>2</sub> saturation is uniform throughout the core (Figure 14) and nearly identical to that of the homogeneous core (Table 3.1).

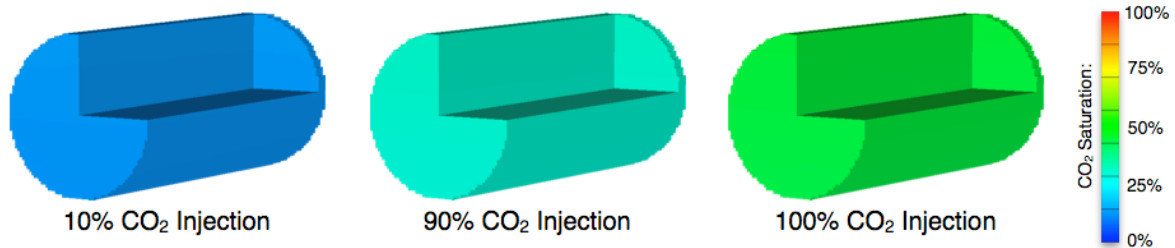


Figure 15: CO<sub>2</sub> saturations of simulated heterogeneous core are identical to those of the homogeneous simulations.

Clearly permeability and porosity variations alone are not the cause of the sub-core scale heterogeneity.

To test the effect of capillary pressure variations, the third scenario used the heterogeneous core and employed Leverett scaling of the elements' capillary pressure curves. This scenario isolates capillary pressure variations as the cause of the sub-core scale CO<sub>2</sub> heterogeneity observed in the lab. The simulation results in Figure 16 show this effect.

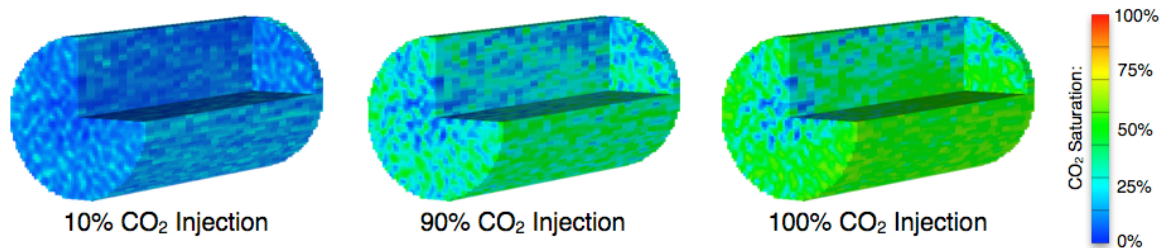


Figure 16: CO<sub>2</sub> saturations of simulated heterogeneous core with variable capillary pressure curves. These simulations exhibit sub-core scale heterogeneity like that observed in the laboratory.

Capillary pressure variations have a dramatic effect on the CO<sub>2</sub> saturation distribution in the core at all three injection proportions. Though the exact distribution is not identical to that of that lab scans, the spatial distribution and magnitude of these sub-core scale variations are qualitatively similar.

Simulation CO<sub>2</sub> saturation profiles (Figure 17) also show a dramatic difference between the saturation profiles of the first two scenarios (which are nearly identical) and the third.

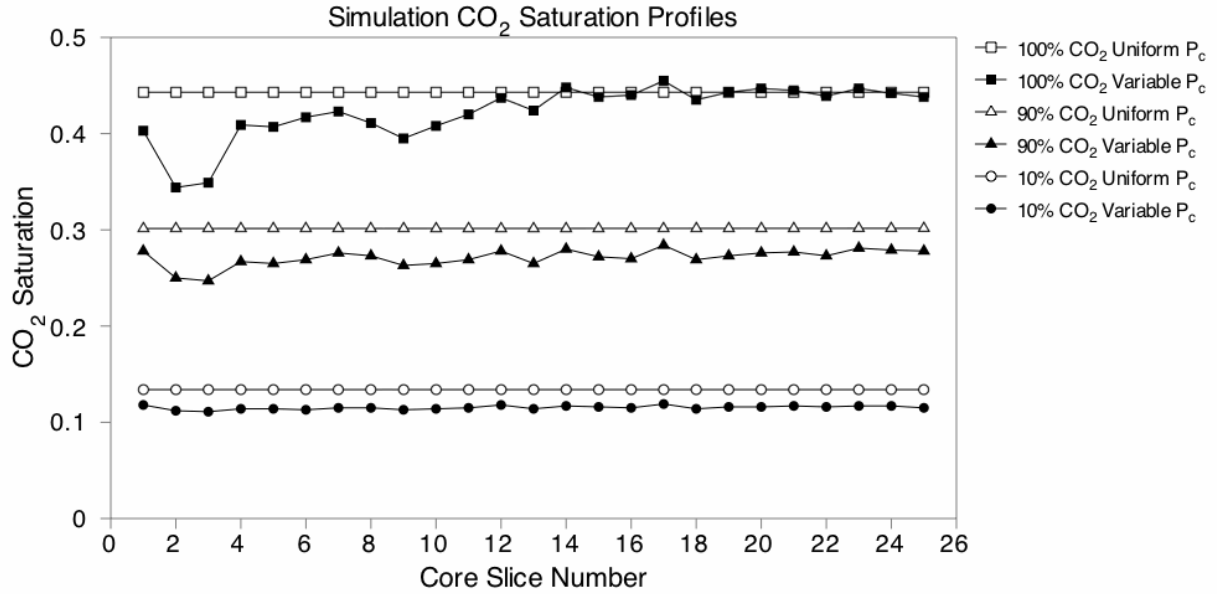


Figure 17: Saturation profiles of simulated scenarios. The first two scenarios have overlapping saturation profiles, so only profiles of scenario two and three are shown.

Capillary pressure curve variations appear to cause a 5 to 15% decrease in average CO<sub>2</sub> saturation (Table I). Leverett scaling requires that areas of lower permeability will have higher capillary entry pressures and areas of higher permeability will have lower capillary entry pressures. Because our core is heterogeneous, areas of high permeability will be more readily invaded by CO<sub>2</sub> while areas of low permeability and high capillary pressure will be bypassed.

Table 3.1: Average core CO<sub>2</sub> saturations for each scenario at three CO<sub>2</sub> injection proportions

	10% CO <sub>2</sub>	90% CO <sub>2</sub>	100% CO <sub>2</sub>
<b>1. Homogeneous Core</b>	13.4%	30.1%	44.3%
<b>2. Heterogeneous Core, Uniform P<sub>c</sub> Curves</b>	13.4%	30.2%	44.4%
<b>3. Heterogeneous Variable P<sub>c</sub> Curves</b>	11.5%	27.1%	42.3%

Though the average CO<sub>2</sub> saturation values from the third scenario are not identical to those in the lab, the third scenario closely reproduces the nature of the observed sub-core scale CO<sub>2</sub> saturation variability.

But what of the non-uniform injection observed at the inlet in the lab experiments? Could this be contributing to or even causing the sub-core scale variations observed? If we compare two simulations (Figure 18), one with uniform injection and the other with

an injection pattern modeled after the experimental results, we see that non-uniform injection does affect the CO<sub>2</sub> distribution throughout the core. However, non-uniform injection alone can not explain much of the sub-core scale CO<sub>2</sub> saturation variations observed. As shown in Figure 19, when we compare the lab results to a uniform capillary pressure simulation with non-uniform injection (Figure 19), we see that non-uniform injection alone cannot produce sub-core scale CO<sub>2</sub> saturation variations. Again, even after accounting for non-uniform injection, variations in capillary pressure are needed to model the “patchy” nature of the observed saturation distributions. Regardless of the CO<sub>2</sub> distribution at the inlet, it seems that a model with variable capillary pressure curves is necessary to replicate sub-core scale CO<sub>2</sub> saturations variations.

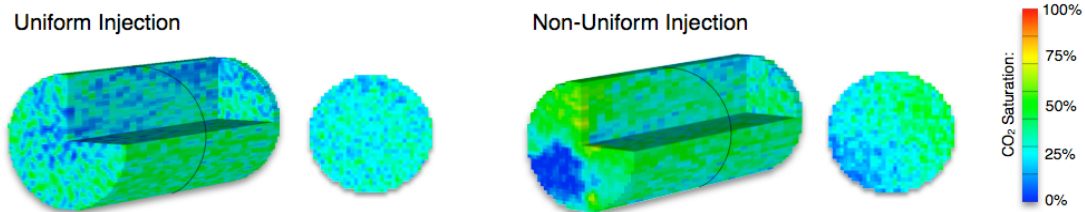


Figure 18: 90% CO<sub>2</sub> / 10% brine simulated injections. Left: Uniform injection identical to that in Figure 16. Right: Non-uniform injection with inlet condition based on lab experiments in Figure 11. In each case, slice 14, mid-way through the core is shown.

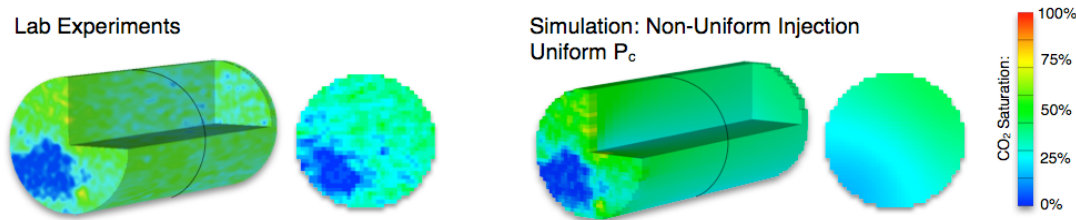


Figure 19: 90% CO<sub>2</sub> / 10% brine injections. Left: Laboratory experiments show that low-CO<sub>2</sub> regions persist through the core. Right: Simulation with uniform capillary pressure curve and non-uniform injection modeled on the lab experiment.

## Discussion

From these results, we foresee two major implications for geologic carbon dioxide storage. First, we hypothesize that CO<sub>2</sub> saturations and brine displacement efficiency could be flow-rate dependent, which would have implications for sweep efficiency of injected CO<sub>2</sub> at large distances from the injection well, where flow-rates are much lower. To test this, we performed four simulated injections of 90% CO<sub>2</sub>/10% brine at the following total flow-rates: 3 mL/min, 0.5 mL/min, 0.1 mL/min, 0.01 mL/min. We observed that steady-state CO<sub>2</sub> saturation is higher for higher flow-rates (Figure 20).

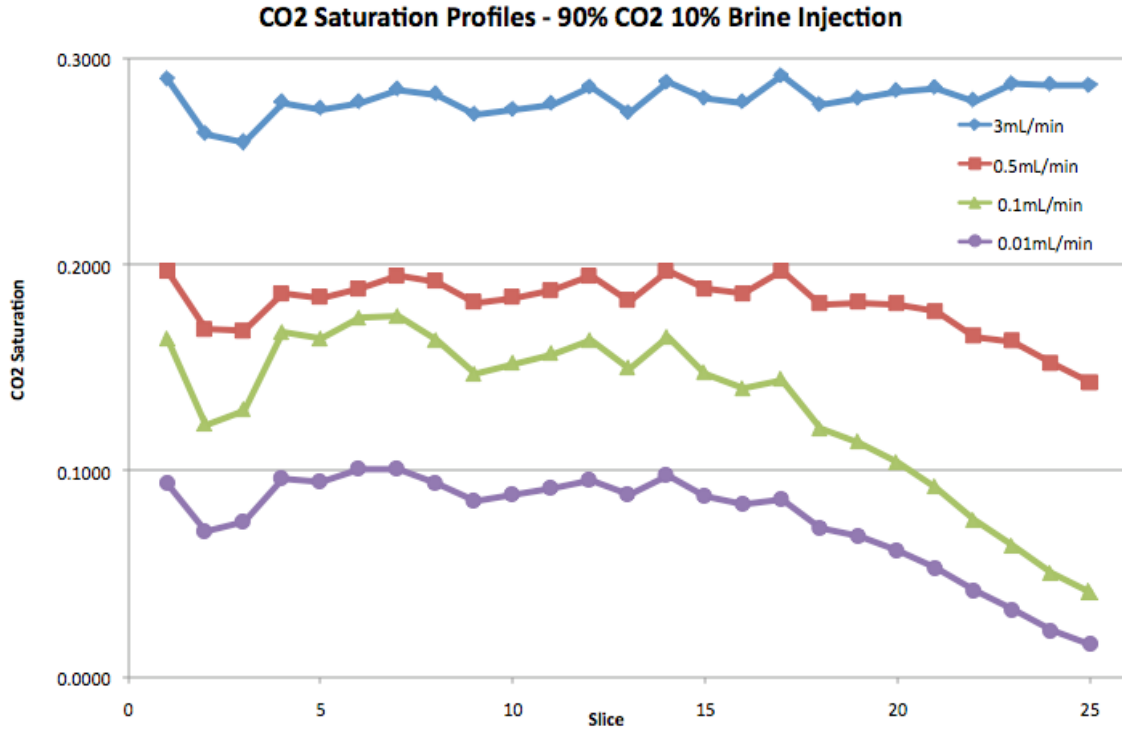


Figure 20: For each simulation, variable capillary pressure curves were used. CO<sub>2</sub> saturation at steady-state varies with injection flow-rate.

To confirm that this flow-rate dependence is not a numerical artifact of time-step size, we ran a representative simulation for 15 seconds of simulated time at four different predefined time-step sizes and observed that the average pressure and CO<sub>2</sub> saturation were the same in all cases (Table 3.2).

Table 3.2: Average pressure and CO<sub>2</sub> saturation given different time-step sizes

Time-step Size (s)	# of Time-steps	Avg. Pressure (MPa)	Avg. CO <sub>2</sub> Saturation
0.5	31	6.9044	0.1550
0.25	66	6.9044	0.1550
0.125	122	6.9044	0.1550
0.0625	243	6.9044	0.1550

Figure 20 shows rather definitively that CO<sub>2</sub> saturation is flow-rate dependent, but what is not immediately clear is why there is a downward trend in CO<sub>2</sub> saturation towards the outlet. Figure 21 shows the outlet-end of the 0.01 mL/min injection simulation at steady-state, where CO<sub>2</sub> does not invade the upper portion of the core. Clearly this is not a gravity affect since brine is denser than CO<sub>2</sub>.

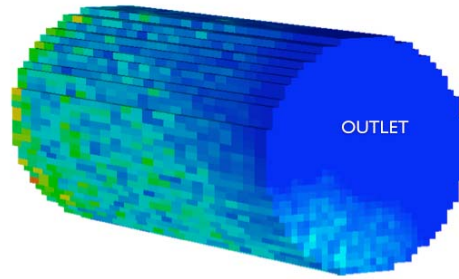


Figure 21: Steady-state view of the outlet-end of the 90% CO<sub>2</sub> / 10% brine, 0.01 mL/min simulation. The core remains un-invaded by CO<sub>2</sub> at the upper-half of the outlet-end.

The answer to this outlet condition lies in a closer examination of the core's permeability distribution. Though the porosity and permeability variations in the core seem evenly distributed to the eye, Figure 22 shows that the top half of the core is significantly less permeable than the bottom half.

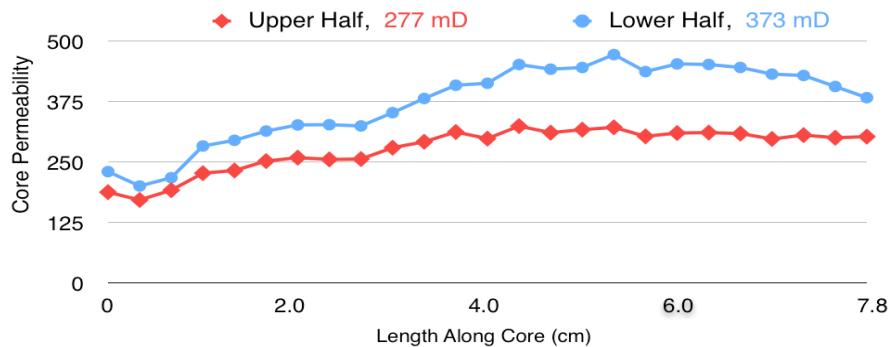


Figure 22: Permeability profiles of the top and bottom halves of the core.

It would appear that CO<sub>2</sub> is finding a preferential flow path in the bottom half of the core and breaking through the outlet there first. Once breakthrough occurs, pressure drops in the core and CO<sub>2</sub> can no longer invade the lower permeability region at the top of the outlet.

Although it does not appear to be affecting the heterogeneous core, gravity override of CO<sub>2</sub> is an important factor to consider. To investigate this phenomenon, we simulated a 100% CO<sub>2</sub> injection into a completely homogeneous core (like that in Figure 15) and ran it to steady-state. We observed that a gravity override seems only to affect low flow-rate simulations.

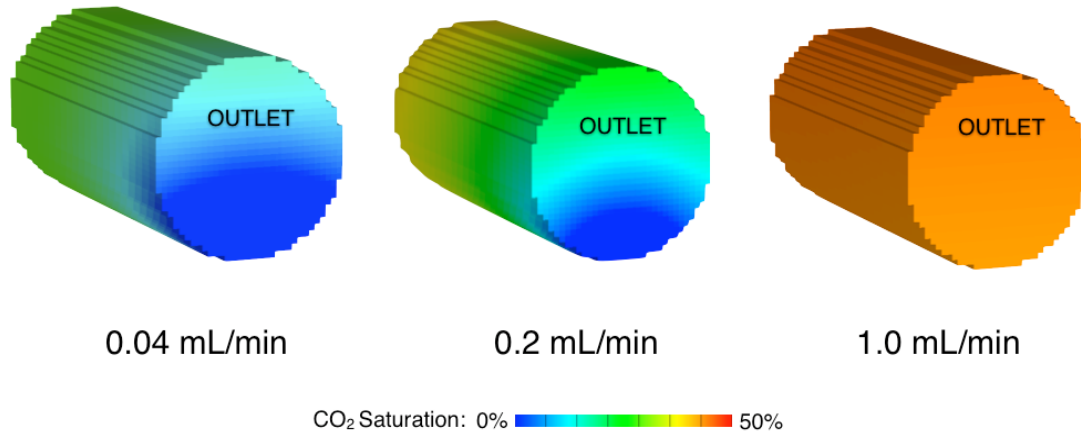


Figure 23: Gravity override is present in the 0.04 mL/min simulation. The effect of gravity decreases when flow-rate is increased to 0.2 mL/min. By 1.0 mL/min, gravity has no effect and CO<sub>2</sub> saturation of the core is uniform.

The second hypothesis deals with the resolution of the simulation grid itself; that is, the coarser the grid resolution, the higher the predicted saturation. The original CT scans have a diameter of 180 pixels. For use in our simulations, we coarsen it to 60 pixels, leaving the number of slices along the length of the core unchanged. Figure 24 shows that had we coarsened it to a diameter of 36 pixels or 18 pixels, our results would have been slightly different.

These results are not entirely surprising. We observed in Figure 17 that a heterogeneous core yields, on average, lower average CO<sub>2</sub> saturations than a homogeneous core of the same average porosity and permeability. The degree of heterogeneity affecting the simulation is directly controlled by the degree of local averaging performed to coarsen the grid. That is, coarser grids are less heterogeneous and produce higher CO<sub>2</sub> saturations.

To confirm that this was not a numerical artifact caused by changing time steps or approximating spatial gradients, we performed a grid resolution test on a homogeneous core. We performed the same 90% CO<sub>2</sub>/10% brine injection at the above three grid diameters: 60 pixels, 36 pixels, 18 pixels. The simulations were run until steady-state when average CO<sub>2</sub> saturation and pressure drop were measured.

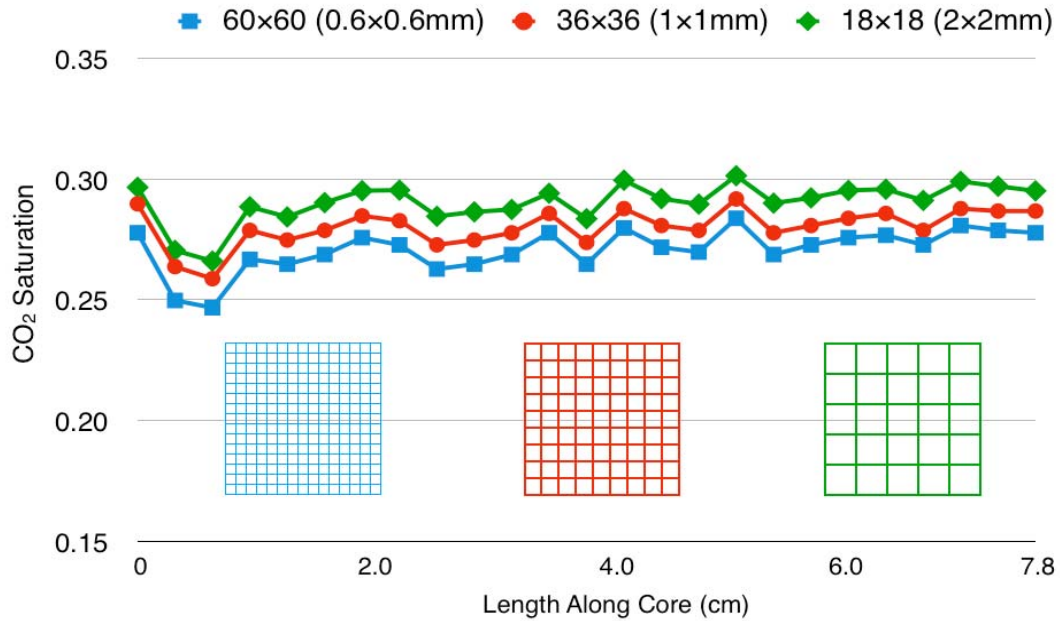
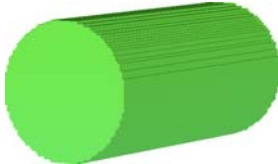
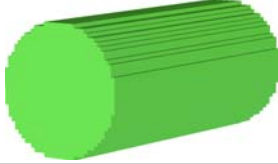
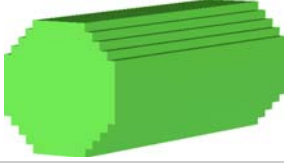



Figure 24: 90% CO<sub>2</sub>/10% brine injection simulations were only simulation grid resolution is varied. Coarser grids produce slightly higher CO<sub>2</sub> saturations. Square grids meant to give a sense of scale to the resolutions.

Table 3.3: Average CO<sub>2</sub> saturation and pressure drop in a homogeneous core of varying diameter resolutions.

Lateral Resolution (voxels)		Average CO <sub>2</sub> Saturation	Pressure Drop (Pa)
60		30.14%	12,677
36		30.13%	12,663
18		30.14%	12,672

CO<sub>2</sub> Saturation: 

The average saturation and pressure drop across the core are unaffected by changes to the lateral grid resolution of the homogeneous core. These results support our

hypothesis that the degree of sub-core scale of heterogeneity in the core as represented by a lateral grid resolution affects average CO<sub>2</sub> saturation. As a final check, we were reassured that the permeability distribution of the core is unaffected by the lateral grid coarsening (see Figure 25).

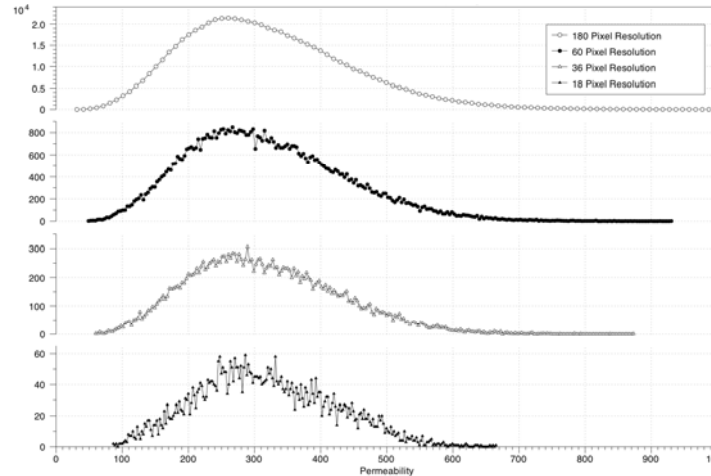


Figure 25: Permeability histograms of the heterogeneous core at various lateral resolutions.

Very little of the permeability distribution appears to be lost by coarsening the grid to 60 pixels in diameter. The 36 and 18 pixels cases also appear to retain much of the histograms structure.

## Conclusions

These numerical investigations suggest that the sub-core scale variations in CO<sub>2</sub> distribution observed in laboratory experiments can only be explained if we consider that each grid-element-sized region of the core has a unique capillary pressure curves determined by that region's porosity and permeability. Moreover, each minute region has a unique capillary entry pressure, making low permeability regions more difficult for CO<sub>2</sub> to invade. We predict a decrease in overall CO<sub>2</sub> saturation at low flow-rates due to lower pressures that do not exceed the capillary entry pressures of low-permeability regions. A similar decrease in overall CO<sub>2</sub> saturation is observed for more highly discretized cores, which exhibit greater permeability ranges than coarser grids.

## Future Plans

Our findings suggest that current understanding of CO<sub>2</sub> flow dynamics may overestimate brine displacement by CO<sub>2</sub> in saline aquifers. These numerical simulations, coupled with laboratory experiments, provide much-needed insights into the workings of CO<sub>2</sub> displacement of brine. The next step in our research is to begin a new series of simulations based on the latest laboratory experiments described in Section 1. These simulations may further support our theory that CO<sub>2</sub> saturation is guided by capillary pressure variations present in heterogeneous rock. Further, we hope to develop a theoretical framework of this capillary pressure relationship so that it can be applied to field-scale simulations, where precise knowledge of rock structure is not known.

## 4. Relative Permeability Explorer

Ljuba Miljkovic: [ljuba@stanford.edu](mailto:ljuba@stanford.edu), Sally M. Benson: [smbenson@stanford.edu](mailto:smbenson@stanford.edu)

Relative permeability curves are essential to the understanding of fundamental CO<sub>2</sub> and brine behavior in storage reservoirs. Currently, there are few published relative permeability curves for CO<sub>2</sub> and brine in the scientific literature, though many labs are now beginning to measure them under various conditions and by a wide variety of experimental methods.

To serve as a resource to the Carbon Capture and Sequestration research community, our group is actively developing a database-backed rich internet application - called the Relative Permeability Explorer (RPE) - to collect and present these relative permeability curves (<http://pangea.stanford.edu/research/bensonlab/relperm/index.html>). Sourced from researcher contributions and peer-reviewed journals, this unique online resource contains complete and searchable metadata — such as rock type, core length, temperature, brine composition, experimental method, etc. — for each set of relative permeability curves, making the tasks of finding and comparing curves very easy.

### Usability

The top half of the application shows a graph of relative permeability curves and information about the sample selected from the data grid below. This area displays characteristics of the rock sample used in the relative permeability measurement, information about the experimental procedure, as well as an abstract and citation for published curves.

The graph values can be examined by moving the cursor over the data points. The fluid phase x-axis can be toggled between CO<sub>2</sub> and brine saturation. All of the data can be downloaded in Excel format by clicking on the downward-pointing arrow in the chart.

All of the rock samples' relative permeability curves are available in the data grid. You can add columns by clicking on the "Add/Remove Columns" button and selecting which columns to show. Rearrange and resize the columns by dragging the headers. You can also sort the data within a column by clicking on its header to explore trends for a particular property.

## **Publications**

### **Referred Journals**

- D. Silin, T. Patzek and S.M. Benson (2008), A model of buoyancy-driven two-phase countercurrent fluid flow. *Transport in porous Media*, in press.
- D. Silin, T. Patzek and S.M. Benson (2008), A model of buoyant gas plume migration, *Journal of Greenhouse Gas Control*, in press.

### **Conference Papers**

- Benson, S.M. (2008). Multi-phase Flow and trapping in Saline Aquifers. Society of Petroleum Engineers, Off-shore Technology Conference. My 5-8, 2008. SPE Paper Number OTC 19244.
- D. Silin, T. Patzek, and S. M. Benson (2008). Modeling evolution of leaking gas plume migration. Groundwater Protection Council Meeting.

### **Abstracts (Submitted and Published)**

- S. M. Benson, L. Miljkovic, L. Tomutsa and C. Doughty, Relative Permeability and Capillary Pressure Controls on CO<sub>2</sub> Migration and Brine Displacement (2007). NETL 6<sup>th</sup> Annual Carbon Sequestration Conference. Pittsburg, PA.
- D. Silin, T. Patzek, and S. M. Benson (2008). Modeling evolution of leaking gas plume migration. Groundwater Protection Council Meeting.
- L. Milkovich and S. M. Benson, Relative Permeability Curve Explorer: A Rich Internet Application (2008). NETL 7<sup>th</sup> Annual Carbon Sequestration Conference. Pittsburg, PA.
- J.-C. Perrin, M. Krause and S. M. Benson (2008), Relative permeability properties of the CO<sub>2</sub> / Brine system in saline aquifers. An experimental study. NETL 7<sup>th</sup> Annual Carbon Sequestration Conference. Pittsburg, PA.
- S. M. Benson (2008) Multi-phase flow of CO<sub>2</sub> and brine in saline aquifers, SEG Annual Meeting.
- L. Miljkovic, C.-W. Kuo, J.-C. Perrin, M. Krause, and S. M. Benson (2008), Numerical Simulations of Laboratory Core-scale CO<sub>2</sub> Displacement Experiments. 9<sup>th</sup> International Greenhouse Gas Control Technology Meeting, Washington D.C.
- J.-C. Perrin, M. Krause, C.-W. Kuo, L. Miljkovic, and S. M. Benson (2008), Relative permeability properties of the CO<sub>2</sub> / Brine system in saline aquifers. 9<sup>th</sup> International Greenhouse Gas Control Technology Meeting, Washington D.C.